



HAL
open science

Mid-infrared emission properties of erbium-doped fluorite-type crystals

Simone Normani, Pavel Loiko, Liza Basyrova, Abdelmjid Benayad, Alain Braud, Elena Dunina, Liudmila Fomicheva, Alexey Kornienko, Ammar Hideur, Patrice Camy

► **To cite this version:**

Simone Normani, Pavel Loiko, Liza Basyrova, Abdelmjid Benayad, Alain Braud, et al.. Mid-infrared emission properties of erbium-doped fluorite-type crystals. *Optical Materials Express*, 2023, 13 (7), pp.1836-1851. 10.1364/OME.482402 . hal-04209389

HAL Id: hal-04209389

<https://hal.science/hal-04209389>

Submitted on 1 Nov 2023

HAL is a multi-disciplinary open access archive for the deposit and dissemination of scientific research documents, whether they are published or not. The documents may come from teaching and research institutions in France or abroad, or from public or private research centers.

L'archive ouverte pluridisciplinaire **HAL**, est destinée au dépôt et à la diffusion de documents scientifiques de niveau recherche, publiés ou non, émanant des établissements d'enseignement et de recherche français ou étrangers, des laboratoires publics ou privés.

Mid-infrared emission properties of erbium-doped fluorite-type crystals

SIMONE NORMANI,¹ PAVEL LOIKO,¹ LIZA BASYROVA,¹ ABDELMJID BENAYAD,¹ ALAIN BRAUD,¹ ELENA DUNINA,² LIUDMILA FOMICHEVA,³ ALEXEY KORNIENKO,² AMMAR HIDEUR,⁴ AND PATRICE CAMY^{1,*}

¹Centre de Recherche sur les Ions, les Matériaux et la Photonique (CIMAP), UMR 6252 CEA-CNRS-ENSICAEN, Université de Caen Normandie, 6 Boulevard Maréchal Juin, 14050 Caen Cedex 4, France

²Vitebsk State Technological University, 210035 Vitebsk, Belarus

³Belarusian State University of Informatics and Radioelectronics, 6 Brovka St., 220027, Minsk, Belarus

⁴CORIA UMR6614, CNRS-INSA-Université de Rouen, Normandie Université, Avenue de l'université, BP. 12, 76801 Saint Etienne du Rouvray, France

*patrice.camy@ensicaen.fr

Abstract: We report on a comparative study of the spectroscopic properties and mid-infrared laser performance of five 5 at.% Er³⁺-doped fluorite-type crystals MF₂, including parent compounds CaF₂, SrF₂, BaF₂, and solid-solution (“mixed”) ones (Ca,Sr)F₂ and (Sr,Ba)F₂. In the M = Ca → Sr → Ba series, the host matrix phonon energy decreases, the absorption and mid-infrared emission spectra of Er³⁺ become narrower and more structured, and the luminescence lifetimes of the ⁴I_{11/2} and ⁴I_{13/2} Er³⁺ manifolds increase. The Er³⁺ transition probabilities were calculated using the Judd-Ofelt theory. In the “mixed” compounds, the Er³⁺ ions tend to reside in the larger / heavier cation environment. The low-temperature (12 K) spectroscopy evidences the presence of a single type of clusters at this doping level; the crystal-field splitting for Er³⁺ ions in clusters was determined. Continuous-wave low-threshold laser operation at ~2.8 μm (the ⁴I_{11/2} → ⁴I_{13/2} transition) was achieved with all five Er³⁺:MF₂ crystals. The maximum achieved laser slope efficiency was 37.9% (Er³⁺:CaF₂), 23.5% (Er³⁺:SrF₂) and 17.2% (Er³⁺:BaF₂).

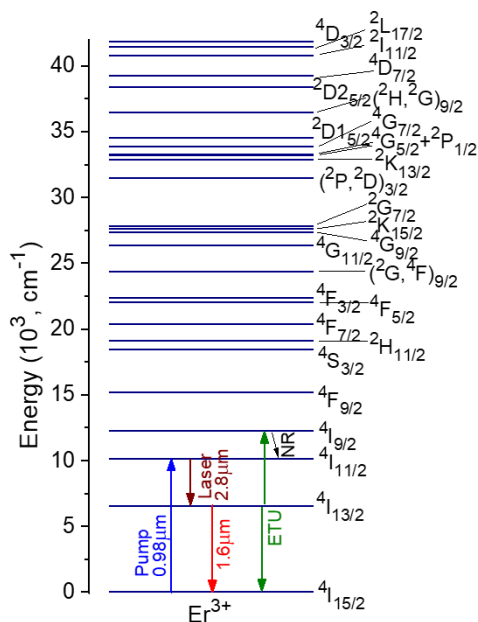
© 2022 Optica Publishing Group under the terms of the [Optica Publishing Group Open Access Publishing Agreement](#)

1. Introduction

Calcium fluoride (CaF₂, also known as fluorite in the mineral form) is a well-known laser host material for doping with trivalent rare-earth ions (RE³⁺) [1-3]. Undoped CaF₂ features good thermal properties (high thermal conductivity and isotropic thermal expansion), low phonon energy, low refractive index and broadband transparency. It also exhibits a unique tendency for strong RE³⁺ ion clustering even at moderate doping concentrations (>0.1 at.%), leading to inhomogeneously broadened spectral bands [4-6]. As a result, the absorption and emission spectra of RE³⁺ ions in CaF₂ greatly resemble those in fluoride glasses being almost structureless and very broad. Such a “glassy-like” spectroscopic behavior is very appealing for broadband wavelength tuning [7,8] and generation of ultrashort pulses in mode-locked lasers [9,10]. The energy-transfer processes among the neighboring RE³⁺ ions (nonradiative energy-transfer, cross-relaxation, and energy-transfer upconversion) are greatly promoted in clusters [11]. This can be used for boosting the efficiency of certain laser transitions of RE³⁺ ions. CaF₂ is a low-melting-point compound. Its growth is well-developed, e.g., by the Czochralski or Bridgman-Stockbarger methods.

CaF₂ belongs to the family of divalent metal fluorides, MF₂ (where M = Ca, Sr, Ba, Cd, or Pb) [12-15]. These materials all belong to the cubic class (sp. gr. *Fm*3⁻*m*, fluorite-type structure). The M²⁺ and F⁻ are located at face-centered cubic lattice points and tetrahedral voids, respectively. Compared to CaF₂, other MF₂ crystals are less studied for RE³⁺ doping but they are also attractive as laser host media as they benefit from either a lower melting point, or better

47 thermal properties, or lower phonon energies. Fluorite-type crystals can also form substitutional
 48 solid-solutions $(M1_{1-x}M2_x)F_2$ for the entire range of $0 < x < 1$ [16-18]. For such “mixed”
 49 compositions, the melting point is expected to decrease further as compared to the parent
 50 compounds [19,20]. An additional spectral broadening is also expected due to the compositional
 51 disorder. The growth and laser operation of some RE^{3+} -doped “mixed” fluorite-type crystals
 52 were reported mainly focusing on $(Ca,Sr)F_2$ [21-23].



53
 54 **Fig. 1.** Energy level scheme of Er^{3+} ions showing all the manifolds assigned in the absorption
 55 spectra of $Er^{3+}:MF_2$ crystals, pump and laser transitions, ETU – energy-transfer upconversion.

53

54

55

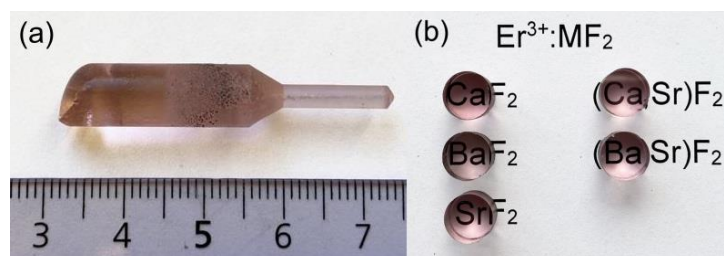
56 Erbium ions (Er^{3+}) are of interest for generation of mid-infrared radiation at $\sim 2.8 \mu\text{m}$ [24,25]
 57 according to the $4I_{11/2} \rightarrow 4I_{13/2}$ transition, Fig. 1. The low-phonon-energy behavior of MF_2 crystals
 58 and the tendency for strong ion clustering promoting the energy-transfer upconversion stimulate
 59 the interest in the development of mid-infrared $Er^{3+}:MF_2$ lasers. Labbe *et al.* first reported on a
 60 mid-infrared 5 at.% $Er^{3+}:\text{CaF}_2$ laser delivering 80 mW at $2.80 \mu\text{m}$ with a slope efficiency of 30%
 61 and a small laser threshold of 23 mW [1]. Basyrova *et al.* demonstrated power scaling of a similar
 62 laser generating 0.83 W at $2.80 \mu\text{m}$ with a slightly higher slope efficiency of 31.6% [26]. In
 63 these studies, high-brightness laser pumping was implemented. Further power scaling was
 64 achieved using commercial InGaAs diode lasers as pump sources. Zong *et al.* developed a
 65 diode-pumped 1.7 at.% $Er^{3+}:\text{CaF}_2$ laser generating 2.32 W at $2.76 \mu\text{m}$ at the expense of a lower
 66 slope efficiency of 21.2% [27]. So far, $Er^{3+}:\text{CaF}_2$ [26,27], $Er^{3+}:\text{SrF}_2$ [28] and $Er^{3+}:(\text{Ca},\text{Sr})F_2$ [23]
 67 crystals have been studied for mid-infrared lasers. Note that $Er^{3+}:\text{CaF}_2$ can also be obtained in
 68 the form of transparent ceramics. Šulc *et al.* reported on a pulsed diode-pumped 5 at.% $Er^{3+}:\text{CaF}_2$
 69 ceramic laser with a broad tuning range of 2687 – 2805 nm (118 nm) [29].

70 Despite the existence of multiple studies for several $Er^{3+}:MF_2$ crystal compositions, their
 71 spectroscopic and mid-infrared laser properties have not been directly compared so far. In the
 72 present work, we report on a comparative study of mid-infrared emission properties of five
 73 fluorite-type Er^{3+} -doped MF_2 crystals, including parent and solid-solution compounds.

74 2. Crystal growth

75 The MF_2 crystals ($M = \text{Ca}, \text{Sr}, \text{Ba}$) melt congruently at relatively low temperatures (cf. Table 1)
 76 and they can be grown by the Bridgman-Stockbarger or Czochralski methods. The $Er^{3+}:MF_2$
 77 crystals were grown by the Bridgman method using graphite crucibles ($\Phi 7\text{-}8 \text{ mm}$, height: 40

78 mm). The MF₂ (M = Ca, Sr, Ba) powders (purity: 4N, Sigma-Aldrich) and ErF₃ powder obtained
 79 by fluorination of the Er₂O₃ precursor (4N, Alfa Aesar). Five compositions were tested: M = Ca,
 80 Sr, Ba, Ca_{0.5}Sr_{0.5} and Sr_{0.5}Ba_{0.5}. The doping level was 5 at.% Er³⁺ (with respect to M²⁺ cations).
 81 The optical quality and spectroscopic properties of RE³⁺-doped MF₂ crystals are sensitive to
 82 even small pollution of oxygen / water in the growth chamber as they can lead to the presence
 83 of oxygen-assisted sites for the dopant ions or even formation of a translucent oxyfluoride phase.
 84 To avoid that, the growth chamber was sealed to vacuum (<10⁻⁵ mbar) and refilled with a mixture
 85 of Ar + CF₄ gases. The starting reagents were well mixed and placed into the crucible which was
 86 then heated slightly above (~30-50 °C) the melting point and the solution was homogenized for
 87 3-4 hours (h). The growth was ensured by a vertical translation of the crucible in a vertical
 88 temperature gradient of 30-40 °C/cm. After the growth was completed, the crystals were cooled
 89 down to room temperature (20 °C) within 48 h.



90
 91 **Fig. 2.** Photographs of Er³⁺:MF₂ crystals: (a) an as-grown Er³⁺:CaF₂ crystal boule; (b) cut and
 92 polished Er³⁺:MF₂ samples.

93 For the “mixed” crystals, the melting point is reduced as compared to those of the parent
 94 compounds. E.g., for Er³⁺:(Ca,Sr)F₂ and Er³⁺:(Sr,Ba)F₂, it is $T_f = 1373$ °C and 1315 °C,
 95 respectively (compare with 1477 °C, 1418 °C and 1386 °C for SrF₂, CaF₂ and BaF₂,
 96 respectively).

97 The as-grown Er³⁺:MF₂ crystals with a cylindrical shape (Φ7-8 mm, length: 35 - 40 mm)
 98 were transparent and rose-colored due to the Er³⁺ doping, Fig. 2(a). Samples for spectroscopic
 99 and laser studies were cut from the central part of the cylindrical barrels with a thickness of 6-7
 100 mm and then polished to laser-grade quality, Fig. 2(b).

101 3. Raman spectra

102 The Raman spectra of Er³⁺:MF₂ crystals, Fig. 3(a), were measured using a confocal microscope
 103 (InVia, Renishaw) equipped with a ×50 Leica objective and an Ar⁺ ion laser (457 nm). Fluorite-
 104 type crystals have O_h symmetry and a triatomic unit cell thus exhibiting only one Raman-active
 105 mode at the center of the Brillouin zone having a T_{2g} symmetry [30]. Indeed, the Raman spectra
 106 of all the studied Er³⁺:MF₂ crystals contain a single intense peak assigned to this vibration.
 107 Frequently, MF₂ crystals may exhibit additional broad Raman bands in the spectral range of 100
 108 – 600 cm⁻¹ owing to structure defects (interstitial / vacant anion sites) [30]. Such a behavior is
 109 not observed in our crystals.

110 For Er³⁺:CaF₂, Er³⁺:SrF₂ and Er³⁺:BaF₂ crystals, the peak frequency of the Raman mode and
 111 its linewidth (FWHM) are 321 / 11.0 cm⁻¹, 285 / 10.2 cm⁻¹ and 242 / 12.0 cm⁻¹, respectively.
 112 Thus, the latter compound is the most favorable one in terms of low-phonon-energy behavior.
 113 For the “mixed” compositions, the Raman peak broadens and is reduced in intensity and the peak
 114 position takes an intermediate place between those for the corresponding parent compounds,
 115 indicating an even distribution of the host-forming cations throughout the structure (a formation
 116 of a substitutional solid-solution) [32]. E.g., for Er³⁺:(Ca,Sr)F₂, the peak Raman frequency is 304
 117 cm⁻¹ and the peak linewidth is 25.9 cm⁻¹.

118 The phonon energy of Er³⁺:MF₂ decreased monotonically with increasing the cationic mass
 119 in agreement with the classical approach, $\nu = (1/2\pi)(k/\mu)^{1/2}$, where k is the force constant and μ
 120 is the reduced mass of the M – F system [33].

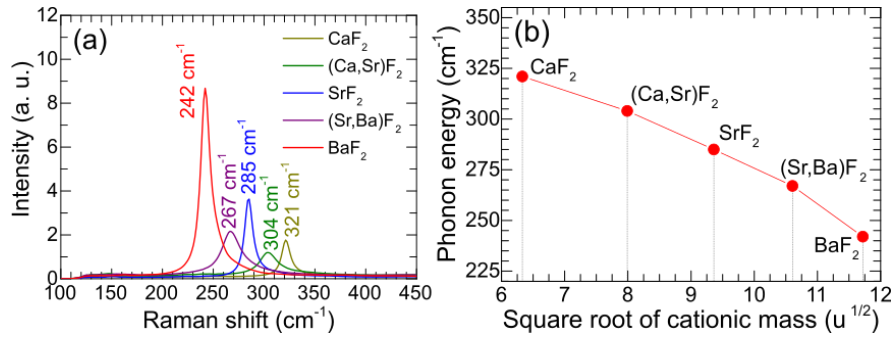


Fig. 3. Raman spectroscopy of Er³⁺:MF₂ crystals: (a) Raman spectra, $\lambda_{\text{exc}} = 457 \text{ cm}^{-1}$, numbers – peak frequencies; (b) phonon energy vs. the square root of the average cationic mass.

121
122
123

4. Optical spectroscopy

4.1 Optical absorption

125
126
127
128
129
130
131
132
133
134
135
136

The absorption spectra of Er³⁺ ions were measured using a spectrophotometer (Lambda 1050, Perkin Elmer). They are shown in Fig. 4. Here, the assignment of Er³⁺ transitions is according to Carnall *et al.* [34]. The absorption spectra for both parent and “mixed” Er³⁺:MF₂ crystals are smooth and broad owing to inhomogeneous spectral broadening caused by a strong ion clustering. In the series M = Ca → Sr → Ba, the complexity and diversity of RE³⁺ ion clusters in MF₂ crystals decrease leading to more intense and structured absorption bands which also exhibit a slight blue-shift [12]. Indeed, for the ⁴I_{15/2} → ⁴I_{11/2} transition, which is used for pumping mid-infrared erbium lasers, the peak absorption cross-section, σ_{abs} , varies from $2.77 \times 10^{-21} \text{ cm}^2$ at 972.3 nm (Er³⁺:BaF₂) to $2.59 \times 10^{-21} \text{ cm}^2$ at 969.5 nm (Er³⁺:SrF₂), to $2.22 \times 10^{-21} \text{ cm}^2$ at 967.6 nm (Er³⁺:CaF₂), while the corresponding absorption bandwidth is 12.9 nm (Er³⁺:BaF₂), 16.9 nm (Er³⁺:SrF₂), and 22.2 nm (Er³⁺:CaF₂).

137
138
139
140
141
142
143
144

A close look at the absorption spectra of “mixed” crystals indicate that there is a great similarity between those of (Er³⁺:(Ca,Sr)F₂ and Er³⁺:SrF₂) and (Er³⁺:(Sr,Ba)F₂ and Er³⁺:BaF₂) ones, suggesting that the dopant ions in such solid-solution compounds tend to reside in clusters with a local surrounding predominantly composed of one of the two host-forming cations (namely, the heavier / larger one – Sr²⁺ or Ba²⁺, respectively). This suggests that Er³⁺ clusters have a tendency to sit in the heavier-cation environment within the solid-solution (M_{1-x}M_{2-x})F₂ crystals. A similar behavior was observed previously for clusters of Nd³⁺/Lu³⁺ ions in “mixed” (Sr,Ba)F₂ crystals [35].

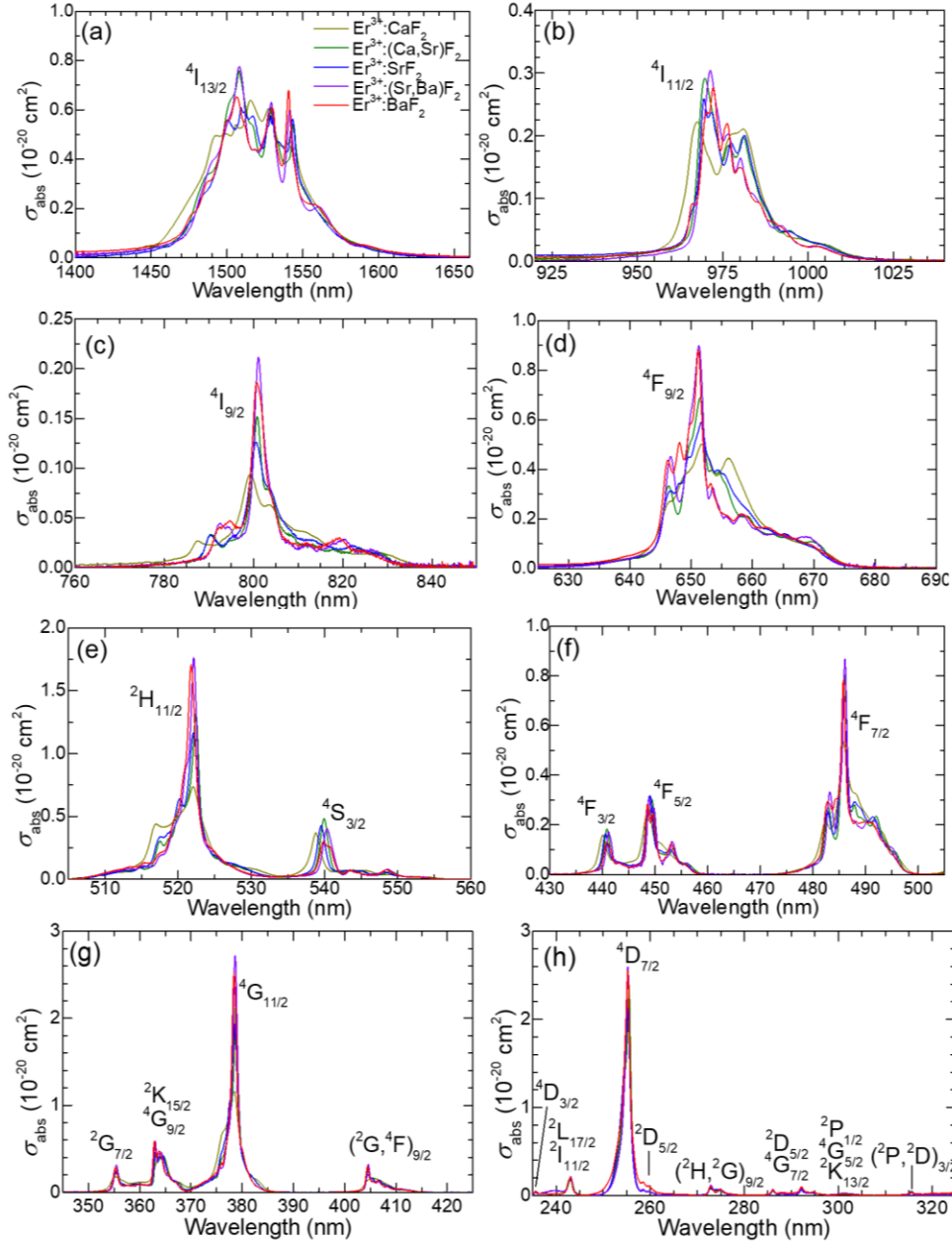
4.2 Judd-Ofelt analysis

145
146
147
148
149
150
151

The measured absorption spectra of Er³⁺ ions in the five studied MF₂ crystals were used to calculate the transition probabilities by means of the standard Judd-Ofelt (J-O) theory [36,37]. The reduced squared matrix elements $U^{(k)}$ ($k = 2, 4, 6$) were calculated using the free-ion parameters from [38]. The magnetic dipole (MD) contributions to transition intensities (for $\Delta J = J - J' = 0, \pm 1$) were calculated within the Russell–Saunders approximation using Er³⁺ wave functions under the free-ion assumption.

152
153
154
155
156
157
158
159
160

Table 1 summarizes the experimental and calculated absorption oscillator strengths (f_{exp} and f_{calc} , respectively) for the three parent compounds, Er³⁺:CaF₂, Er³⁺:SrF₂ and Er³⁺:BaF₂. There exists a direct relation between the absorption oscillator strength / integrated absorption cross-section and the radiative lifetime of the excited-state (the principle of reciprocity, referring to Einstein coefficients). For Er³⁺ transitions from the ground-state (⁴I_{15/2}) to the two lower-lying excited-states (⁴I_{13/2} and ⁴I_{11/2}), the f_{calc} value decreases in the M = Ca → Sr → Ba series, so that an opposite tendency is expected for the radiative lifetimes of these two states. The root mean square (r.m.s.) deviation between the f_{exp} and f_{calc} values is relatively low for all the tested Er³⁺:MF₂ crystals, lying in the range of 0.137 – 0.257.



161
162

Fig. 4. (a-h) Absorption spectra of Er³⁺ ions in MF₂ crystals.

163 The J-O (intensity) parameters Ω_2 , Ω_4 , Ω_6 for Er³⁺ ions in MF₂ crystals are listed in Table 2.
 164 The determined J-O parameters were used to calculate the probabilities of spontaneous
 165 radiative transitions of Er³⁺ ions. In Table 3, we list the parameters relevant for mid-infrared
 166 laser operation, i.e., the radiative lifetimes τ_{rad} of the ⁴I_{13/2} and ⁴I_{11/2} states and the luminescence
 167 branching ratio $\beta_{JJ'}$ for the ⁴I_{11/2} → ⁴I_{13/2} transition. As expected, in the M = Ca → Sr → Ba
 168 series, the τ_{rad} values for the considered excited-states tend to increase from 7.09 / 6.53 ms
 169 (Er³⁺:CaF₂) to 7.57 / 6.99 ms (Er³⁺:SrF₂) and further to 7.52 / 7.11 ms (Er³⁺:BaF₂). The
 170 considered $\beta_{JJ'}$ value is also higher for Sr²⁺ and Ba²⁺-containing crystals.

171

Table 1. Absorption Oscillator Strengths^a for Er³⁺ Ions in Parent MF₂ (M = Ca, Sr, Ba) Crystals

Transition	Er ³⁺ :CaF ₂		Er ³⁺ :SrF ₂		Er ³⁺ :BaF ₂	
	$f_{\text{exp}}, \times 10^{-6}$	$f_{\text{calc}}, \text{J-O}, \times 10^{-6}$	$f_{\text{exp}}, \times 10^{-6}$	$f_{\text{calc}}, \text{J-O}, \times 10^{-6}$	$f_{\text{exp}}, \times 10^{-6}$	$f_{\text{calc}}, \text{J-O}, \times 10^{-6}$
⁴ I _{15/2} → ^{2S+1} L _J						
⁴ I _{13/2}	2.496	1.643 ^{ED} + 0.448 ^{MD}	2.129	1.510 ^{ED} + 0.448 ^{MD}	2.220	1.404 ^{ED} + 0.461 ^{MD}
⁴ I _{11/2}	0.714	0.693 ^{ED}	0.643	0.631 ^{ED}	0.598	0.592 ^{ED}
⁴ I _{9/2}	0.333	0.229 ^{ED}	0.328	0.283 ^{ED}	0.343	0.333 ^{ED}
⁴ F _{9/2}	2.264	2.139 ^{ED}	2.217	2.283 ^{ED}	2.265	2.406 ^{ED}
⁴ S _{3/2} + ² H _{11/2}	3.531	3.366 ^{ED}	3.422	3.544 ^{ED}	4.387	4.760 ^{ED}
⁴ F _{7/2}	2.141	2.454 ^{ED}	2.396	2.342 ^{ED}	2.205	2.236 ^{ED}
⁴ F _{5/2} + ² F _{3/2}	1.266	1.300 ^{ED}	1.114	1.173 ^{ED}	0.962	1.056 ^{ED}
² G _{9/2}	0.898	0.970 ^{ED}	0.637	0.902 ^{ED}	0.603	0.840 ^{ED}
⁴ G _{11/2} + ² K _{15/2} + ⁴ G _{9/2} + ² G _{7/2}	7.888	7.917 ^{ED} + 0.053 ^{MD}	8.585	8.474 ^{ED} + 0.053 ^{MD}	11.400	11.168 ^{ED} + 0.055 ^{MD}
r.m.s. dev.		0.217		0.137		0.234

172

173

^a f_{exp} and f_{calc} - experimental and calculated absorption oscillator strengths, respectively, ED – electric dipole, MD – magnetic dipole.

174

Table 2. Judd-Ofelt Parameters of Er³⁺ Ions in MF₂ Crystals

Host crystal	$\Omega_2, 10^{-20} \text{ cm}^2$	$\Omega_4, 10^{-20} \text{ cm}^2$	$\Omega_6, 10^{-20} \text{ cm}^2$
CaF ₂	1.436	1.364	1.892
(Ca,Sr)F ₂	1.244	1.483	1.720
SrF ₂	1.477	1.701	1.701
(Sr,Ba)F ₂	1.519	1.836	1.529
BaF ₂	2.397	1.964	1.487

175

Table 3. Selected Probabilities^a of Spontaneous Radiative Transitions of Er³⁺ in MF₂ crystals

Host crystal	$\tau_{\text{rad}}(^4\text{I}_{13/2}), \text{ ms}$	$\tau_{\text{rad}}(^4\text{I}_{11/2}), \text{ ms}$	$\beta_{\text{Jr}}(^4\text{I}_{11/2} \rightarrow ^4\text{I}_{13/2}), \%$
CaF ₂	7.09	6.53	14.9
(Ca,Sr)F ₂	7.64	7.06	15.8
SrF ₂	7.57	6.99	16.0
(Sr,Ba)F ₂	7.90	7.56	16.5
BaF ₂	7.52	7.11	16.1

176

^a τ_{rad} – radiative lifetime, β_{Jr} – luminescence branching ratio.

177

4.3 Emission spectra and luminescence lifetimes

178

179

180

181

182

The luminescence spectra of Er³⁺ ions in the mid-infrared (the ⁴I_{11/2} → ⁴I_{13/2} transition) were measured using an optical spectrum analyzer (OSA, Yokogawa AQ6376) and a ZrF₄ fiber. The excitation source was a Ti:Sapphire laser tuned to ~970 nm. The OSA was purged with N₂ gas. To remove the effect of the residual water vapor absorption in air, the set-up was calibrated using a 20 W quartz iodine lamp.

183

184

The stimulated-emission (SE) cross-sections, σ_{SE} , were calculated using the Füchtbauer-Ladenburg equation [39]:

185

$$\sigma_{\text{SE}}(\lambda) = \frac{\lambda^5}{8\pi \langle n \rangle^2 \tau_{\text{rad}} c} \frac{B(\text{Jr})W(\lambda)}{\int \lambda W(\lambda) d\lambda}, \quad (1)$$

186

187

188

189

where λ is the light wavelength, $\langle n \rangle$ is the refractive index of the crystal at the mean emission wavelength, τ_{rad} corresponds to the ⁴I_{11/2} state and β_{Jr} – to the ⁴I_{11/2} → ⁴I_{13/2} transition (cf. Table 3), c is the speed of light, and $W(\lambda)$ is the measured luminescence spectrum corrected for the response of the set-up.

190

191

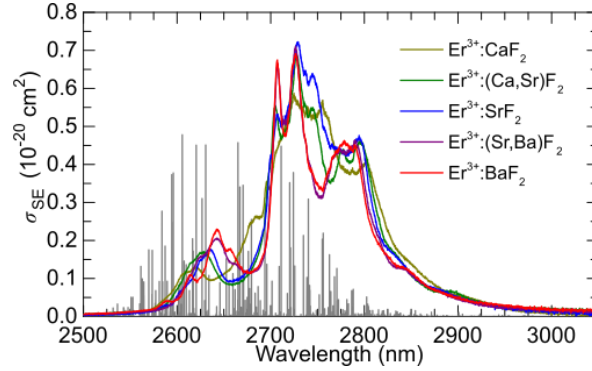
192

193

194

The SE cross-section spectra for Er³⁺ ions in MF₂ crystals are shown in Fig. 5. Similarly to the absorption spectra, a profound inhomogeneous broadening is observed for both the parent and “mixed” Er³⁺:MF₂ crystals owing to the rare earth ion clustering. For all the studied crystals, the emission spectra are very broad extending from 2.55 to 3.05 μm and the main emission peak appears around 2.72 μm . Such a behavior is beneficial for broadly tunable and potentially

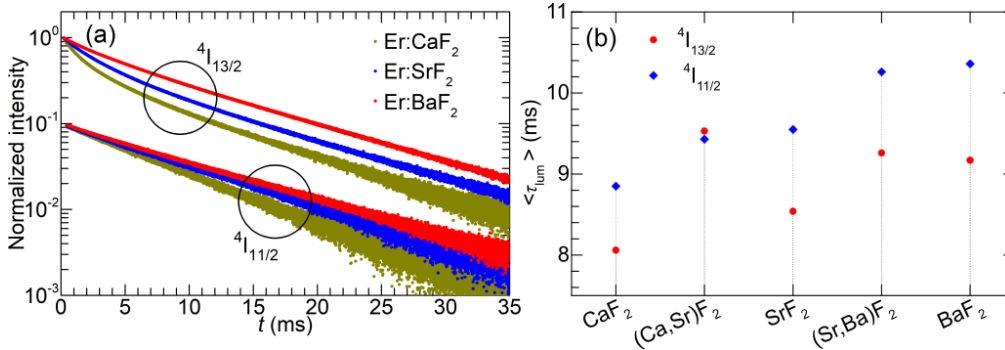
195 mode-locked lasers. The spectra become more structured in the $M = \text{Ca} \rightarrow \text{Sr} \rightarrow \text{Ba}$ series.
 196 Also for the solid-solution compounds, a great similarity between the emission spectra of
 197 $(\text{Er}^{3+}:(\text{Ca,Sr})\text{F}_2$ and $\text{Er}^{3+}:\text{SrF}_2)$ and $(\text{Er}^{3+}:(\text{Sr,Ba})\text{F}_2$ and $\text{Er}^{3+}:\text{BaF}_2)$ crystals is observed.



198
 199 **Fig. 5.** Stimulated-emission (SE) cross-sections, σ_{SE} , for the ${}^4\text{I}_{11/2} \rightarrow {}^4\text{I}_{13/2}$ Er^{3+}
 200 transition in MF_2 crystals, corrected for the structured water vapor absorption in air (in *grey*, arb. units, according
 201 to the HITRAN database).

202 The highest SE cross-section is observed for $\text{Er}^{3+}:\text{SrF}_2$, $\sigma_{\text{SE}} = 7.19 \times 10^{-21} \text{ cm}^2$ at 2729 nm
 203 and at longer wavelengths, two other intense and broad peaks appear ($\sigma_{\text{SE}} = 6.38 \times 10^{-21} \text{ cm}^2$ at
 204 2745 nm and $4.69 \times 10^{-21} \text{ cm}^2$ at 2794 nm).

205 Luminescence decays were studied under resonant excitation using a ns optical parametric
 206 oscillator (Horizon, Continuum), a 1/4 m monochromator (Oriel 77200), an InGaAs detector
 207 and an 8 GHz oscilloscope (DSA70804B, Tektronix). To reduce the reabsorption (radiation
 208 trapping) effect on the measured kinetics, the samples were finely ground into powders. The
 209 measured luminescence decay curves from the ${}^4\text{I}_{13/2}$ and ${}^4\text{I}_{11/2}$ Er^{3+} states in the three parent
 210 crystals, CaF_2 , SrF_2 and BaF_2 , are shown in Fig. 6(a). They deviate from the single-exponential
 211 law (especially for ${}^4\text{I}_{13/2}$) owing to the strong ETU from these long-living states. Thus, the mean
 212 luminescence lifetimes $\langle \tau_{\text{lum}} \rangle = \int t \cdot I(t) dt / \int I(t) dt$ were determined.



213
 214 **Fig. 6.** Luminescence dynamics from the ${}^4\text{I}_{13/2}$ and ${}^4\text{I}_{11/2}$ Er^{3+} manifolds in MF_2 crystals: (a)
 215 luminescence decay curves under resonant excitation of Er^{3+} ions in CaF_2 , SrF_2 , and BaF_2 , $\lambda_{\text{exc}} =$
 216 $1.48 \mu\text{m}$, $\lambda_{\text{lum}} = 1.57 \mu\text{m}$ (the ${}^4\text{I}_{13/2}$ state), $\lambda_{\text{exc}} = 0.97 \mu\text{m}$, $\lambda_{\text{lum}} = 1.01 \mu\text{m}$ (the ${}^4\text{I}_{11/2}$ state); (b) mean
 217 luminescence lifetimes $\langle \tau_{\text{lum}} \rangle$ as a function of the host composition.

218 The summary of the $\langle \tau_{\text{lum}} \rangle$ values for the five studied $\text{Er}^{3+}:\text{MF}_2$ crystals is given in Fig. 6(b).
 219 With increasing the average radius / atomic mass of the M^{2+} host-forming cations (in the $M =$
 220 $\text{Ca} \rightarrow \text{Sr} \rightarrow \text{Ba}$ series), and, accordingly, decreasing the phonon energy of the host matrix, both
 221 the ${}^4\text{I}_{13/2}$ and ${}^4\text{I}_{11/2}$ luminescence lifetimes tend to increase, from 8.06 / 8.85 ms ($\text{Er}^{3+}:\text{CaF}_2$) to
 222 8.54 / 9.55 ms ($\text{Er}^{3+}:\text{SrF}_2$) and further to 9.17 / 10.36 ms ($\text{Er}^{3+}:\text{BaF}_2$). This behavior agrees with
 223 that for the calculated radiative lifetimes of these manifolds. The ratio of the upper-to-lower

224 laser level lifetimes is favorable for all the studied crystals being weakly dependent on the host
 225 matrix composition. The long luminescence lifetime of the upper laser level for the mid-infrared
 226 transition (${}^4I_{11/2}$) is a prerequisite for a low-threshold behavior.

227 Note that the measured luminescence lifetimes are slightly exceeding the radiative ones
 228 calculated using the J-O theory (cf. Table 3). One possible reason for that is the residual
 229 reabsorption effect within the Er^{3+} ion clusters.

230

Table 4. Spectroscopic Characteristics^a of $\text{Er}^{3+}:\text{MF}_2$ Crystals

Parameter / Crystal	CaF_2	$(\text{Ca,Sr})\text{F}_2$	SrF_2	$(\text{Sr,Ba})\text{F}_2$	BaF_2
λ_{abs} , nm	967.6	969.7	969.5	971.4	972.3
σ_{abs} , 10^{-21} cm^2	2.22	2.91	2.59	3.04	2.77
λ_{em} , nm	2724.8	2727.6	2728.9	2726.6	2726.5
σ_{SE} , 10^{-21} cm^2	5.87	6.90	7.22	7.11	6.92
$\langle\tau_{\text{lum}}\rangle({}^4I_{13/2})$, ms	8.06	9.53	8.54	9.26	9.17
$\langle\tau_{\text{lum}}\rangle({}^4I_{11/2})$, ms	8.85	9.43	9.55	10.26	10.36

231

232

^a λ_{abs} , λ_{em} – peak absorption / emission wavelengths, respectively, σ_{abs} , σ_{SE} – peak absorption / SE cross-sections, respectively, $\langle\tau_{\text{lum}}\rangle$ - average luminescence lifetime.

233

4.4 Low-temperature spectroscopy

234

235

236

237

238

239

For low-temperature (LT, 12 K) absorption and luminescence studies, we have used an APD DE-202 closed-cycle cryo-cooler equipped with an APD HC 2 Helium vacuum cryo-compressor and a Laceshore 330 temperature controller. For absorption measurements, a 20 W quartz lamp with a calibrated spectral output was used. The spectra were measured using optical spectrum analyzers (Ando AQ6315A and Yokogawa AQ6375E). The luminescence was excited by a Ti:Sapphire laser tuned to ~ 800 nm.

240

241

242

243

244

245

The LT absorption and emission spectra are shown in Fig. 7 and Fig. 8, respectively. In each graph, we compare the spectrum of a “mixed” compound with those of both parent crystals. The LT absorption spectra were plotted versus the phonon energy giving access to the splitting of the ${}^4I_{13/2}$ and ${}^4I_{11/2}$ excited-states, while the LT emission spectra were plotted versus ($E_{\text{ZPL}} - \text{photon energy}$), where E_{ZPL} is the zero-phonon line (ZPL) energy giving access to the splitting of the ground-state ${}^4I_{15/2}$.

246

247

248

249

250

251

252

253

254

255

256

By analyzing the spectra, several conclusions can be derived:

257

258

259

260

261

262

263

264

265

266

267

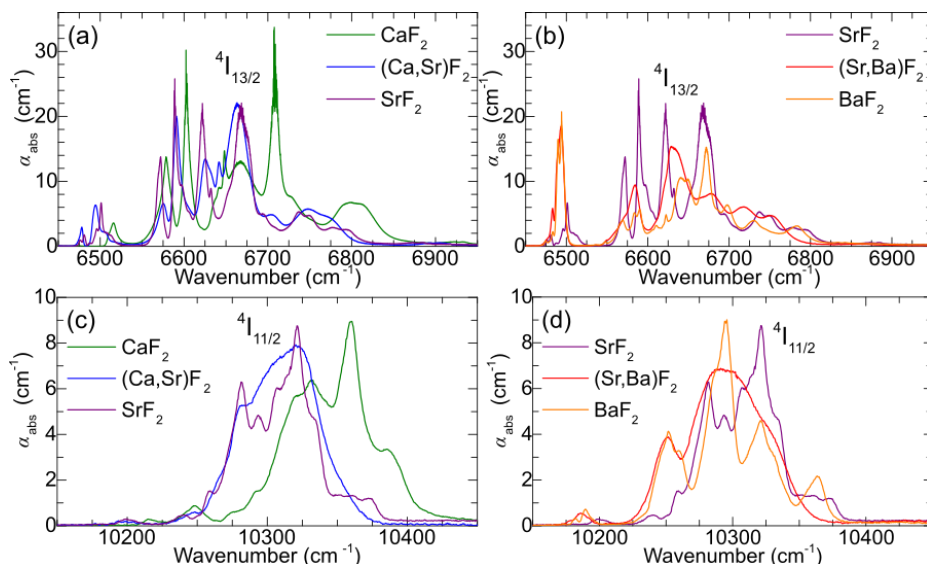
(i) The absorption and emission spectra of Er^{3+} ions in MF_2 crystals contain very broad bands even at 12 K indicating a significant inhomogeneous spectral broadening due to the rare-earth ion clustering. The spectra become more structured in the series $\text{M} = \text{Ca} \rightarrow \text{Sr} \rightarrow \text{Ba}$ indicating smaller variety of cluster geometries;

(ii) The spectra of “mixed” fluorite-type crystals exhibit additional broadening as compared to the corresponding parent compounds due to the presence of two different host-forming cations. The spectra of such “mixed” crystals are more similar to those of the heavier-cation parent (e.g., $(\text{Ca,Sr})\text{F}_2$ and SrF_2 , $(\text{Ba,Sr})\text{F}_2$ and BaF_2). This corroborates the observation made in Section 4.3, confirming that the majority of Er^{3+} ions tend to reside in the vicinity of heavier cations within “mixed” crystals;

(iii) The total Stark splitting of Er^{3+} multiplets in clusters in MF_2 crystals decreases in the $\text{M} = \text{Ca} \rightarrow \text{Sr} \rightarrow \text{Ba}$ series, and the corresponding barycenter energies experience a progressive red-shift. The strength of the crystal-field is expected to be larger for smaller sites (shorter $\text{M} - \text{F}$ and $\text{M} - \text{M}$ distances, in our case) due to the stronger lattice distortion on the dopant ion. Indeed, the lattice constant increases in the series CaF_2 (5.45 Å) \rightarrow SrF_2 (5.80 Å) \rightarrow BaF_2 (6.20 Å).

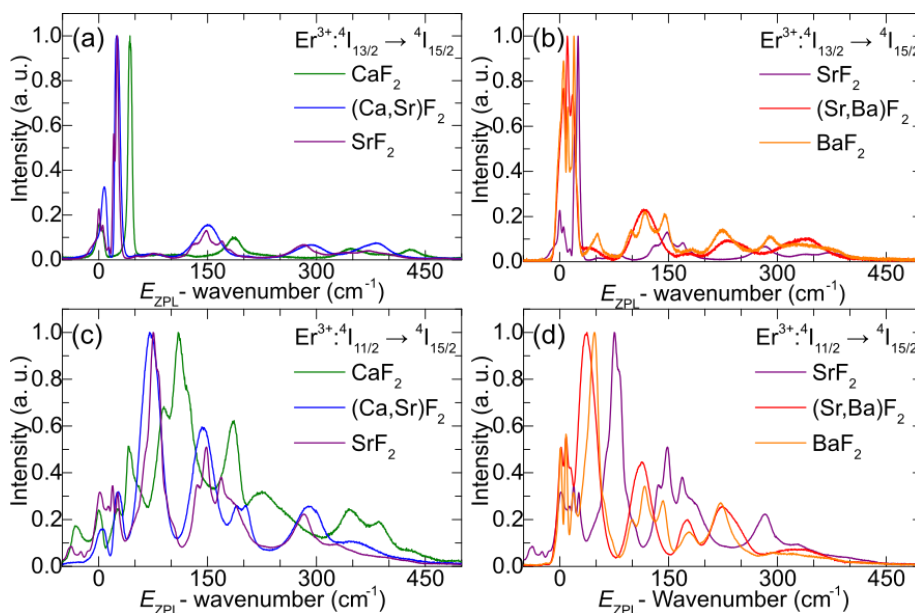
Based on the LT absorption and emission spectra, the crystal-field splitting of the ${}^4I_{15/2}$, ${}^4I_{13/2}$ and ${}^4I_{11/2}$ multiplets of Er^{3+} ions forming clusters in the three parent MF_2 crystals ($\text{M} = \text{Ca}, \text{Sr}, \text{Ba}$), was determined, Table 5. The experimental Stark splitting of the ${}^4I_{11/2}$ and ${}^4I_{13/2}$ multiplets relevant for the 2.8 μm laser operation is also compared in Fig. 9. In the previous studies on site-selective spectroscopy of Er^{3+} ions in CaF_2 crystals grown under oxygen-free atmosphere, multiple possible sites were identified [40-42]. At very low doping levels (<0.05 at.%), the Er^{3+}

268 ions are mostly isolated and are distributed over tetragonal (A, C_{4v}), trigonal (B, C_{3v}) and cubic
 269 (O_h) sites, depending on the relative position of the charge-compensating interstitial fluorine anion
 270 (F_i^-), namely at the (1,0,0) positions, at the (1,1,1) positions or sufficiently far from the dopant ion
 271 to exert negligible perturbation, respectively [40]. For higher doping levels of >0.1 at.%, the
 272 dopant ions form clusters of several types (assigned as C-sites, being close to dimers with a
 273 distorted C_{3v} symmetry, and D(1) and D(2) sites corresponding to larger agglomerates of Er^{3+} -
 274 F_i^- pairs).



275
 276
 277

Fig. 7. (a-d) LT (12 K) absorption spectra of Er^{3+} ions in fluorite-type crystals: (a,b) the ${}^4I_{15/2} \rightarrow {}^4I_{13/2}$ transition; (c,d) ${}^4I_{15/2} \rightarrow {}^4I_{11/2}$ transition. α_{abs} – absorption coefficient.



278
 279
 280

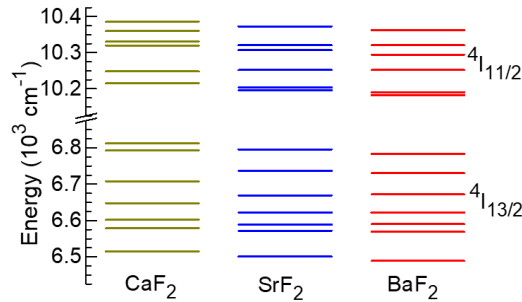
Fig. 8. (a-d) LT (12 K) luminescence spectra of Er^{3+} ions in fluorite-type crystals: (a,b) the ${}^4I_{13/2} \rightarrow {}^4I_{15/2}$ transition; (c,d) ${}^4I_{11/2} \rightarrow {}^4I_{15/2}$ transition. E_{ZPL} – zero-phonon-line energy.

281 For the studied heavily doped $\text{Er}^{3+}:\text{MF}_2$ crystals, we were not able to confirm the existence of
 282 two significantly different groups of ion clusters (D(1) and D(2)), as the LT emission spectra were
 283 almost independent on the excitation wavelength. Moreover, the bands in the LT spectra of ~ 5
 284 at.% Er^{3+} -doped crystals (assigned to a single type of cluster D sites) experience an additional
 285 broadening and spectral shifts as compared to those in 0.1 at.% Er^{3+} -doped crystals (assigned to
 286 D(1) and D(2) sites). Thus, we assumed that almost all the Er^{3+} ions form large-scale agglomerates
 287 (D) with relatively close spectroscopic properties. Previously, it was suggested that for all the
 288 heavily doped MF_2 crystals ($M = \text{Ca}, \text{Sr}, \text{Ba}$) and their solid-solutions, such agglomerates most
 289 likely correspond to hexameric Y_6F_{37} superstructure units, which are nearly identical in volume
 290 and shape to the Ca_2F_{32} building blocks of the fluorite lattice and, consequently, they can be
 291 easily incorporated into this lattice while accommodating the excess F_i^- anions [5,43]. The local
 292 crystal-field symmetry for the dopant ions in Y_6F_{37} clusters is tetragonal (C_{4v}) [5].

293

Table 5. Crystal-Field Splitting of Selected Er^{3+} Multiplets in CaF_2 , SrF_2 , and BaF_2

Crystal	Er^{3+} $^{2S+1}L_J$	Sub-level / Energy (cm^{-1})							
		1	2	3	4	5	6	7	8
CaF_2	$^4I_{15/2}$	0	42	90	110	186	228	346	387
	$^4I_{13/2}$	6516	6579	6602	6648	6708	6793	6812	
	$^4I_{11/2}$	10215	10248	10320	10331	10360	10386		
SrF_2	$^4I_{15/2}$	0	25	63	75	148	187	283	330
	$^4I_{13/2}$	6501	6572	6589	6622	6669	6737	6796	
	$^4I_{11/2}$	10196	10204	10282	10307	10321	10373		
BaF_2	$^4I_{15/2}$	0	18	34	48	117	142	222	293
	$^4I_{13/2}$	6489	6569	6590	6622	6672	6730	6784	
	$^4I_{11/2}$	10182	10190	10252	10295	10321	10363		



294

295

296

Fig. 9. Experimental Stark splitting of the $^4I_{11/2}$ and $^4I_{13/2}$ multiplets of Er^{3+} ions forming clusters in heavily doped $\text{Er}^{3+}:\text{MF}_2$ crystals.

297

298

The analysis of Table 2 confirms a decreased total Stark splitting of the multiplets and a red-shift of the zero-phonon line for Er^{3+} ions in the $M = \text{Ca} \rightarrow \text{Sr} \rightarrow \text{Ba}$ series.

299

5. Laser operation

300

5.1 Laser setup

301

302

303

304

305

306

307

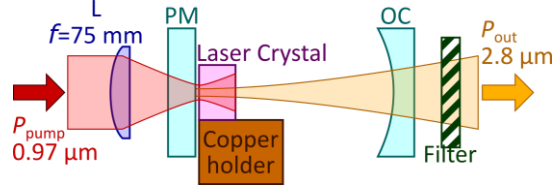
308

309

310

The scheme of the laser set-up is shown in Fig. 10. Cylindrical samples with a thickness of 6.53-6.99 mm and a diameter of ~ 7 mm were cut from the central parts of the as-grown $\text{Er}^{3+}:\text{MF}_2$ crystal boules. They were polished to laser-grade quality with good parallelism ($< 5^\circ$) from both sides and left uncoated. The laser elements were mounted on a passively cooled Cu-holder using a silver paint for better heat removal. A hemispherical cavity was implemented. It was formed by a flat pump mirror (PM) coated for high transmission (HT, $T = 85.7\%$) at $0.97 \mu\text{m}$ and high reflection (HR) at $2.6 - 3.0 \mu\text{m}$, and a set of concave (radius of curvature: $\text{RoC} = -100 \text{ mm}$) output couplers (OC) having a transmission T_{OC} in the range of 0.33% - 4% at $2.7 - 2.9 \mu\text{m}$. The crystal was placed near the PM at a small distance ($< 1 \text{ mm}$). The geometrical cavity length was $\sim 99 \text{ mm}$. The pump source was a CW Ti:Sapphire laser delivering up to 3.2 W at $0.97 \mu\text{m}$

311 (addressing the ${}^4I_{15/2} \rightarrow {}^4I_{11/2}$ Er^{3+} absorption peak) with a diffraction-limited beam quality (M^2
 312 ≈ 1). The pump radiation was focused into the laser crystal through the PM using an
 313 antireflection-coated achromatic lens (focal length: $f = 75$ mm) resulting in a pump spot size of
 314 $2w_p = 66 \pm 5$ μm . The pumping was in single pass. The residual (non-absorbed) pump after the
 315 OC was filtered out using a long-pass filter (Spectrogon, LP1400). The laser spectra were
 316 measured using a ZrF_4 fiber (Thorlabs) and a spectrum analyzer (Bristol, 771 series). The laser
 317 mode profile in the far-field was captured using a camera (Pyrocam IIIHR, Ophir-Spiricon).

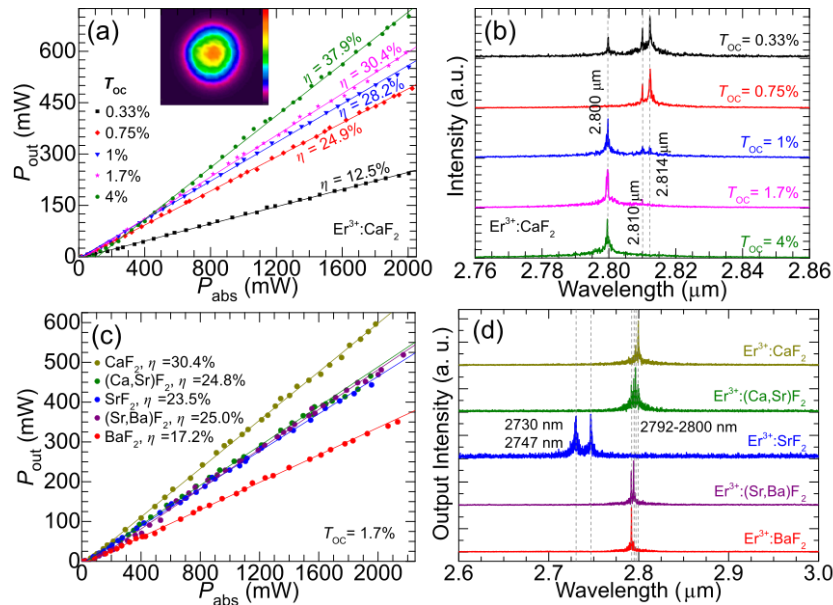


318
 319
 320

Fig. 10. Schematic of the laser setup: L – aspherical focusing lens; PM – flat pump mirror; OC – curved output coupler.

321 5.2 Laser performance

322 CW mid-infrared laser operation was obtained with all five studied $\text{Er}^{3+}:\text{MF}_2$ crystals. The best
 323 laser performance was achieved with the $\text{Er}^{3+}:\text{CaF}_2$ crystal: an output power of 702 mW was
 324 extracted at 2800 nm with a slope efficiency η of 37.9% (vs. the absorbed pump power) when
 325 using the output coupler with $T_{\text{OC}} = 4\%$, Fig. 11(a). With increasing output coupling from 0.33%
 326 to 4%, the laser threshold gradually increased from 16 mW to 60 mW. For $\text{Er}^{3+}:\text{CaF}_2$, the
 327 measured pump absorption reached 81.9%. The optical-to-optical efficiency (vs. the pump power
 328 incident on the crystal) η_{opt} was 31.0%. The output dependences were linear within the studied
 329 range of pump powers. Further power scaling was limited by the available pump. The achieved
 330 laser slope efficiency is slightly higher than the Stokes limit, $\eta_{\text{St,L}} = \lambda_p/\lambda_L = 34.6\%$, indicating the
 331 role of the ETU process ${}^4I_{13/2} + {}^4I_{13/2} \rightarrow {}^4I_{9/2} + {}^4I_{15/2}$, cf. Fig. 1, refilling the upper laser level and
 332 depopulating the intermediate ${}^4I_{13/2}$ state.



333
 334
 335
 336
 337

Fig. 11. Mid-infrared $\text{Er}^{3+}:\text{MF}_2$ lasers: (a,b) $\text{Er}^{3+}:\text{CaF}_2$ laser: (a) input-output dependences, η – slope efficiency, *inset* – far-field mode profile, $P_{\text{abs}} \sim 1.5$ W, $T_{\text{OC}} = 1.7\%$; (b) typical laser spectra; (c,d) a comparison of (c) power transfer characteristics and (d) laser spectra for five $\text{Er}^{3+}:\text{MF}_2$ crystals, $T_{\text{OC}} = 1.7\%$.

338 The typical emission spectra of the $\text{Er}^{3+}:\text{CaF}_2$ laser are shown in Fig. 11(b), measured well
 339 above the laser threshold. For small output coupling (<1%), laser emission at 2810 and 2814 nm
 340 was observed and for higher T_{OC} , the laser operated at 2800 nm. These wavelengths correspond
 341 to the long-wave emission peak of Er^{3+} ions in CaF_2 and match the transparency ranges between
 342 the structured water vapor absorption lines (cf. Fig. 5). Note that due to strong resonant excited-
 343 state absorption from the terminal laser level with a non-negligible population, ${}^4\text{I}_{13/2} \rightarrow {}^4\text{I}_{11/2}$,
 344 causing reabsorption of the laser photons, the ${}^4\text{I}_{11/2} \rightarrow {}^4\text{I}_{13/2}$ Er^{3+} laser transition represents a
 345 quasi-three-level laser scheme with reabsorption, which explains the blue-shift of the laser
 346 spectra with increasing the output coupling.

347 The $\text{Er}^{3+}:\text{CaF}_2$ laser operated on the fundamental transverse mode, as confirmed by the
 348 measured $M^2 < 1.1$, and the beam profile in the far-field was nearly circular, see the inset in
 349 Fig. 11(a).

350 The output performance and laser spectra of five $\text{Er}^{3+}:\text{MF}_2$ crystals are directly compared in
 351 Fig. 11(c,d) using the same output coupling ($T_{\text{OC}} = 1.7\%$). The slope efficiency gradually
 352 decreased in the sequence $\text{Er}^{3+}:\text{CaF}_2 \rightarrow \text{Er}^{3+}:\text{SrF}_2$ and Sr-containing crystals $\rightarrow \text{Er}^{3+}:\text{BaF}_2$, while
 353 the laser threshold was in the range of 17 – 28 mW for all the crystals, being only slightly higher
 354 for Ba-containing ones. The laser emission occurred at 2792 – 2800 nm, except of $\text{Er}^{3+}:\text{SrF}_2$ for
 355 which the laser operated at shorter wavelengths, 2730 and 2747 nm. The output characteristics
 356 of mid-infrared $\text{Er}^{3+}:\text{MF}_2$ lasers are summarized in Table 6. More details about the 2.8 μm laser
 357 performance of Ba-containing crystals can be found in [44].

358

Table 6. Output Characteristics^a of Mid-Infrared $\text{Er}^{3+}:\text{MF}_2$ Lasers ($T_{\text{OC}} = 1.7\%$)

Parameter / Crystal	CaF_2	$(\text{Ca,Sr})\text{F}_2$	SrF_2	$(\text{Sr,Ba})\text{F}_2$	BaF_2
t , mm	6.81	6.99	6.53	6.99	6.66
λ_p , nm	967.8	969.7	969.5	971.4	971.2
η_{abs} , %	81.9	84.3	76.1	83.3	83.8
P_{out} , mW	596	466	443	519	350
λ_L , nm	2800	2796	2747	2794	2792
P_{th} , mW	20	17	20	28	26
η , %	30.4	24.8	23.5	25.0	17.2

359

^a t – crystal thickness, λ_p – pump wavelength, η_{abs} – pump absorption under lasing conditions,

360

P_{out} – output power, λ_L – laser wavelength, P_{th} – laser threshold, η – slope efficiency.

361

6. Conclusions

362

Fluorite-type $\text{Er}^{3+}:\text{MF}_2$ parent and solid-solution crystals feature low-phonon-energy behavior,
 363 very broad absorption and mid-infrared emission spectral bands, owing to the profound Er^{3+} ion
 364 clustering and long ${}^4\text{I}_{11/2}$ and ${}^4\text{I}_{13/2}$ luminescence lifetimes. As for the “mixed” compounds, their
 365 advantage is the lower melting points with respect to the corresponding parents. Considering the
 366 high thermal conductivity of these materials, the $\text{Er}^{3+}:\text{MF}_2$ crystals are very promising for the
 367 development of power-scalable and broadly tunable low-threshold mid-infrared lasers emitting at
 368 $\sim 2.8 \mu\text{m}$. Based on a detailed comparative spectroscopic study of five 5 at.% $\text{Er}^{3+}:\text{MF}_2$ fluorite-
 369 type crystals, including the parent compounds CaF_2 , SrF_2 , BaF_2 , and “mixed” ones, $(\text{Ca,Sr})\text{F}_2$
 370 and $(\text{Sr,Ba})\text{F}_2$, the following conclusions are derived:

371

(i) The phonon energy of $\text{Er}^{3+}:\text{MF}_2$ crystals monotonously decreases with the square root of
 372 the M^{2+} cationic mass, from 321 cm^{-1} ($\text{Er}^{3+}:\text{CaF}_2$) to 242 cm^{-1} ($\text{Er}^{3+}:\text{BaF}_2$). Such a low-phonon
 373 energy behavior is a prerequisite for almost vanishing multiphonon non-radiative path from
 374 both the ${}^4\text{I}_{11/2}$ and ${}^4\text{I}_{13/2}$ Er^{3+} manifolds, as confirmed by the luminescence decay studies and the
 375 Judd-Ofelt analysis yielding the radiative lifetimes;

376

(ii) In the $M = \text{Ca} \rightarrow \text{Sr} \rightarrow \text{Ba}$ series, the absorption and mid-infrared emission spectra
 377 gradually become narrower and more structured, which is linked to the decreasing complexity
 378 of Er^{3+} clusters, and the luminescence lifetimes of the ${}^4\text{I}_{13/2} / {}^4\text{I}_{11/2}$ Er^{3+} manifolds increase, from
 379 8.06 / 8.85 ms ($\text{Er}^{3+}:\text{CaF}_2$) to 9.17 / 10.36 ms ($\text{Er}^{3+}:\text{BaF}_2$) because of a decrease in the crystal

380 field strength. The observed ratio of the upper-to-lower laser level lifetimes and their values are
381 favorable for low-threshold mid-infrared laser operation;

382 (iii) The Er^{3+} ions in “mixed” crystals tend to reside in a local environment predominantly
383 composed of the larger / heavier M^{2+} cations, leading to a great similarity between the spectra
384 of $\text{Er}^{3+}:\text{SrF}_2$ and $\text{Er}^{3+}:(\text{Ca},\text{Sr})\text{F}_2$, $\text{Er}^{3+}:\text{BaF}_2$ and $\text{Er}^{3+}:(\text{Sr},\text{Ba})\text{F}_2$. At LT, the spectra of Er^{3+} ions
385 in solid-solution crystals exhibit a notable inhomogeneous broadening;

386 (iv) For the doping level of 5 at.% Er^{3+} in MF_2 crystals, the LT spectroscopy reveals the
387 existence of a single class of Er^{3+} clusters with rather close absorption / emission properties (D
388 centers), contrary to crystals with low doping levels subject to ion clustering of various nature
389 (D(1) and D(2)).

390 In the present work, we employed high-brightness pumping to reveal the potential of
391 $\text{Er}^{3+}:\text{MF}_2$ crystals for efficient lasing at $\sim 2.8 \mu\text{m}$. Further power scaling is envisioned by using
392 powerful InGaAs laser diodes as pump sources which is feasible owing to the good thermal
393 properties of these compounds. Further improvement of the slope efficiency, especially for Sr
394 and Ba-containing crystals should involve an optimization of the Er^{3+} doping level for boosting
395 the ETU efficiency. One hypothesis here is that a reduction in the cluster complexity may lead
396 to weaker energy-transfer processes. Another idea is the $\text{Er}^{3+},\text{Pr}^{3+}$ codoping for quenching the
397 metastable Er^{3+} lower-laser level (${}^4\text{I}_{13/2}$).

398 **Funding.** French Agence Nationale de la Recherche (ANR) SPLENDID2 (ANR-19-CE08-0028). “RELANCE”
399 Chair of Excellence project funded by the Normandy Region.

400 **Disclosures.** The authors declare no conflicts of interest.

401 **Data availability.** Data underlying the results presented in this paper are not publicly available at this time but may
402 be obtained from the authors upon reasonable request.

403 References

- 404 1. C. Labbe, J. L. Doualan, P. Camy, R. Moncorgé, and M. Thuau, “The 2.8 μm laser properties of Er^{3+} doped
405 CaF_2 crystals,” *Opt. Commun.* **209**(1-3), 193-199 (2002).
- 406 2. F. Druon, S. Ricaud, D. N. Papadopoulos, A. Pellegrina, P. Camy, J. L. Doualan, R. Moncorgé, A. Courjaud, E.
407 Mottay and P. Georges, “On $\text{Yb}:\text{CaF}_2$ and $\text{Yb}:\text{SrF}_2$: review of spectroscopic and thermal properties and their
408 impact on femtosecond and high power laser performance,” *Opt. Mater. Express* **1**(3), 489-502 (2011).
- 409 3. P. Camy, J. L. Doualan, S. Renard, A. Braud, V. Ménard, and R. Moncorgé, “ $\text{Tm}^{3+}:\text{CaF}_2$ for 1.9 μm laser
410 operation,” *Opt. Commun.* **236**(4-6), 395-402 (2004).
- 411 4. V. Petit, P. Camy, J.-L. Doualan, X. Portier, and R. Moncorgé, “Spectroscopy of $\text{Yb}^{3+}:\text{CaF}_2$: from isolated
412 centers to clusters,” *Phys. Rev. B* **78**(8), 085131-1-12 (2008).
- 413 5. S. A. Kazanskii, and A. I. Ryskin, “Group-III Ion Clusters in Activated Fluorite-Like Crystals,” *Phys. Solid
414 State* **44**(8), 1415-1425 (2002).
- 415 6. B. Lacroix, C. Genevois, J. L. Doualan, G. Brasse, A. Braud, P. Ruterana, P. Camy, E. Talbot, R. Moncorgé,
416 and J. Margerie, “Direct imaging of rare-earth ion clusters in $\text{Yb}:\text{CaF}_2$,” *Phys. Rev. B* **90**(12), 125124-1-14
417 (2014).
- 418 7. V. Petit, J. L. Doualan, P. Camy, V. Ménard and R. Moncorgé, “CW and tunable laser operation of Yb^{3+} doped
419 CaF_2 ,” *Appl. Phys. B* **78**(6), 681-684 (2004).
- 420 8. R. Thouroude, A. Tyazhev, A. Hideur, P. Loiko, P. Camy, J. L. Doualan, H. Gilles, and M. Laroche, “Widely
421 tunable in-band-pumped $\text{Tm}:\text{CaF}_2$ laser,” *Opt. Lett.* **45**(16), 4511-4514 (2020).
- 422 9. G. Machinet, P. Seviliano, F. Guichard, R. Dubrasquet, P. Camy, J. L. Doualan, R. Moncorgé, P. Georges, F.
423 Druon, D. Descamps and E. Cormier, “High-brightness fiber laser-pumped 68 fs-2.3 W Kerr-lens mode-locked
424 $\text{Yb}:\text{CaF}_2$ oscillator,” *Opt. Lett.* **38**(9), 4008-4010 (2013).
- 425 10. A. Lucca, G. Debourg, M. Jacquemet, F. Druon, F. Balembos, P. Georges, P. Camy, J. L. Doualan and R.
426 Moncorgé, “High-power diode-pumped $\text{Yb}^{3+}:\text{CaF}_2$ femtosecond laser,” *Opt. Lett.* **29**(23), 2767-2769 (2004).
- 427 11. P. Loiko, A. Braud, L. Guillemot, J.L. Doualan, A. Benayad, and P. Camy, “Cross-relaxation and ion clustering
428 in $\text{Tm}^{3+}:\text{CaF}_2$ crystals,” *Proc. SPIE* **11357**, 113570N (2020).
- 429 12. P. Camy, J. L. Doualan, A. Benayad, M. Von Edlinger, V. Ménard and R. Moncorgé, “Comparative
430 spectroscopic and laser properties of Yb^{3+} -doped CaF_2 , SrF_2 and BaF_2 single crystals,” *Appl. Phys. B* **89**(4),
431 539-542 (2007).
- 432 13. S. Bordj, H. Satha, A. Barros, D. Zambon, J. P. Jouart, M. Diaf, M., and R. Mahiou, “Spectroscopic
433 characterization by up conversion of $\text{Ho}^{3+}/\text{Yb}^{3+}$ codoped CdF_2 single crystal” *Opt.Mater.* **118**, 111249 (2021).
- 434 14. M. Zhou, P. Zhang, X. Niu, J. Liao, Q. Chen, S. Zhu, Y. Hang, Q. Yang, H. Yin, Z. Li, and Z. Chen, “Ultra-
435 broadband and enhanced near-infrared emission in Bi/Er co-doped PbF_2 laser crystal,” *J. Alloys Compd.* **895**,
436 162704 (2022).

- 437
438
439
440
441
442
443
444
445
446
447
448
449
450
451
452
453
454
455
456
457
458
459
460
461
462
463
464
465
466
467
468
469
470
471
472
473
474
475
476
477
478
479
480
481
482
483
484
485
486
487
488
489
490
491
492
493
494
495
15. W. Z. Xue, Z. L. Lin, H. J. Zeng, G. Zhang, P. Loiko, L. Basyrova, A. Benayad, P. Camy, V. Petrov, X. Mateos, L. Wang, and W. Chen, "Diode-pumped mode-locked Yb:BaF₂ laser," *Opt. Express* **30**(9), 15807-15818 (2022).
 16. S. V. Kuznetsov, V. A. Konyushkin, A. N. Nakladov, E. V. Chernova, P. A. Popov, A. A. Pynenkov, K. N. Nishchev, and P. P. Fedorov, "Thermophysical properties of single crystals of CaF₂-SrF₂-RF₃ (R= Ho, Pr) fluorite solid solutions," *Inorg. Mater.* **56**(9), 975-981 (2020).
 17. P. P. Fedorov, I. I. Buchinskaya, N. A. Ivanovskaya, V. V. Konvalova, S. V. Lavrishchev, and B. P. Sobolev, "CaF₂-BaF₂ phase diagram," *Dokl. Phys. Chem.* **401**(4), 53-55. Nauka/Interperiodica (2025).
 18. P. A. Popov, A. A. Krugovoykh, V. A. Konyushkin, A. N. Nakladov, S. V. Kuznetsov, and P. P. Fedorov, "Thermal Conductivity of Sr_{1-x}Ba_xF₂ Single Crystals," *Inorg. Mater.* **57**(6), 629-633 (2021).
 19. D. Klimm, M. Rabe, R. Bertram, R. Uecker, and L. Parthier, "Phase diagram analysis and crystal growth of solid solutions Ca_{1-x}Sr_xF₂," *J. Cryst. Growth* **310**(1), 152-155 (2008).
 20. R. H. Nafziger, "High-Temperature Phase Relations in the System BaF₂-SrF₂," *J. Am. Ceram. Soc.* **54**(9), 467-467 (1971).
 21. J. L. Doualan, P. Camy, A. Benayad, V. Ménard, R. Moncorgé, J. Boudeile, F. Druon, F. Balembois, and P. Georges, "Yb³⁺ doped (Ca,Sr,Ba)F₂ for high power laser applications," *Laser Phys.* **20**(2), 533-536 (2010).
 22. K. Veselský, J. Šulc, H. Jelínková, M. E. Doroshenko, V. A. Konyushkin, and A. N. Nakladov, "Spectroscopic and laser properties of a broadly tunable diode-pumped Tm³⁺:CaF₂-SrF₂ laser," *Laser Phys. Lett.* **17**(2), p.025802 (2020).
 23. J. Liu, X. Feng, X. Fan, Z. Zhang, B. Zhang, J. Liu, and L. Su, "Efficient continuous-wave and passive Q-switched mode-locked Er³⁺:CaF₂-SrF₂ lasers in the mid-infrared region," *Opt. Lett.* **43**(10), 2418-2421 (2018).
 24. B. J. Dinerman and P. F. Moulton, "3- μ m cw laser operations in erbium-doped YSGG, GGG, and YAG," *Opt. Lett.* **19**(15), 1143-1145 (1994).
 25. G. A. Newburgh, and M. Dubinskii, "Power and efficiency scaling of Er:ZBLAN fiber laser," *Laser Phys. Lett.* **18**(9), 095102-1-6 (2021).
 26. L. Basyrova, P. Loiko, J. L. Doualan, A. Benayad, A. Braud, B. Viana, and P. Camy, "Thermal lensing, heat loading and power scaling of mid-infrared Er:CaF₂ lasers," *Opt. Express* **30**(5), 8092-8103 (2022).
 27. M. Zong, Y. Wang, Z. Zhang, J. Liu, L. Zhao, J. Liu, and L. Su, "High-power 2.8 μ m lasing in a lightly-doped Er: CaF₂ crystal," *J. Lumin.* **250**, 119089 (2022).
 28. R. Švejkar, J. Šulc, H. Jelínková, V. Kubeček, W. Ma, D. Jiang, Q. Wu, and L. Su, "Diode-pumped Er:SrF₂ laser tunable at 2.7 μ m," *Opt. Mater. Express* **8**(4), 1025-1030 (2018).
 29. J. Šulc, M. Němec, R. Švejkar, H. Jelínková, M. E. Doroshenko, P. P. Fedorov, and V. V. Osiko, "Diode-pumped Er:CaF₂ ceramic 2.7 μ m tunable laser," *Opt. Lett.* **38**(17), 3406-3409 (2013).
 30. J. P. Russell, "The Raman spectrum of calcium fluoride," *Proc. Phys. Soc.* (1958-1967), **85**(1), p.194 (1965).
 31. L. Su, J. Xu, W. Yang, X. Jiang, and Y. Dong, "Raman spectra of undoped and uranium doped CaF₂ single crystals," *Chin. Opt. Lett.* **3**(4), 219-221 (2005).
 32. R. K. Chang, B. Lacina, and P. S. Pershan, "Raman scattering from mixed crystals (Ca_xSr_{1-x})F₂ and (Sr_xBa_{1-x})F₂," *Phys. Rev. Lett.* **17**(14), 755 (1966).
 33. A. Ubaldini, and M. M. Carnasciali, "Raman characterisation of powder of cubic RE₂O₃ (RE= Nd, Gd, Dy, Tm, and Lu), Sc₂O₃ and Y₂O₃," *J. Alloys Compd.* **454**(1-2), 374-378 (2008).
 34. W. T. Carnall, P. R. Fields, and K. Rajnak, "Electronic energy levels in the trivalent lanthanide aquo ions. I. Pr³⁺, Nd³⁺, Pm³⁺, Sm³⁺, Dy³⁺, Ho³⁺, Er³⁺, and Tm³⁺," *J. Chem. Phys.* **49**(10), 4424-4442 (1968).
 35. S. Normani, "Nd,Lu:CaF₂ for high-energy lasers" (Doctoral dissertation, Normandie Université) (2017).
 36. B. R. Judd, "Optical Absorption Intensities of Rare-Earth Ions," *Phys. Rev.* **127**(3), 750-761 (1962).
 37. G. S. Ofelt, "Intensities of Crystal Spectra of Rare-Earth Ions," *J. Chem. Phys.* **37**(3), 511-520 (1962).
 38. P. A. Tanner, V. R. K. Kumar, C. K. Jayasankar, and M. F. Reid, "Analysis of spectral data and comparative energy level parametrizations for Ln³⁺ in cubic elpasolite crystals," *J. Alloys Compd.* **215**(1-2), 349-370 (1994).
 39. B. Aull, and H. Jenssen, "Vibronic interactions in Nd:YAG resulting in nonreciprocity of absorption and stimulated emission cross sections," *IEEE J. Quantum Electron.* **18**, 925-930 (1982).
 40. J. B. Fenn Jr, J. C. Wright, and F. K. Fong, "Optical study of ion-defect clustering in CaF₂: Er³⁺," *J. Chem. Phys.* **59**(10), 5591-5599 (1973).
 41. D. R. Tallant, and J. C. Wright, "Selective laser excitation of charge compensated sites in CaF₂: Er³⁺," *J. Chem. Phys.* **63**(5), 2074-2085 (1975).
 42. D.S. Moore, and J.C. Wright, "Laser spectroscopy of defect chemistry in CaF₂: Er³⁺," *J. Chem. Phys.* **74**(3), 1626-1636 (1981).
 43. A. E. Nikiforov, A. Y. Zakharov, M. Y. Ugryumov, S. A. Kazanskii, A. I. Ryskin, and G. S. Shakurov, "Crystal fields of hexameric rare-earth clusters in fluorites," *Phys. Solid State* **47**(8), 1431-1435 (2005).
 44. S. Normani, L. Basyrova, P. Loiko, A. Benayad, A. Braud, A. Hideur, and P. Camy, "Mid-infrared laser operation of Er³⁺-doped BaF₂ and (Sr,Ba)F₂ crystals," *Opt. Lett.* **48**(2), 431-434 (2023).